Spatiotemporal characteristics of uniform momentum zones
Experiments and modeling

Laskari, Angeliki; De Silva, Charitha M.; Hutchins, Nicholas; Mckeon, Beverley J.

DOI
10.1103/PhysRevFluids.7.104603

Publication date
2022

Document Version
Final published version

Published in
Physical Review Fluids

Spatiotemporal characteristics of uniform momentum zones: Experiments and modeling

Angeliki Laskari [1,*] Charitha M. de Silva [2] Nicholas Hutchins,[3] and Beverley J. McKeon [4]
[1]*Department of Process and Energy, Delft University of Technology, 2628 CD Delft, The Netherlands*
[2]*School of Mechanical and Manufacturing Engineering, University of New South Wales, Sydney NSW 2052, Australia*
[3]*Department of Mechanical Engineering, University of Melbourne, Melbourne VIC 3052, Australia*
[4]*Graduate Aerospace Laboratories, California Institute of Technology, Pasadena, California 91125, USA*

(Received 15 February 2022; accepted 9 September 2022; published 7 October 2022)

The probability density function (PDF) of the instantaneous streamwise velocity has consistently been used to extract information on the formation of uniform momentum zones (UMZs) in wall-bounded flows. Its temporal evolution has previously revealed patterns associated with the geometry and amplitude of the underlying velocity fluctuations [Laskari and McKeon, J. Fluid Mech. **913**, A6 (2021)]. In this paper, we examine the robustness of these patterns in a variety of data sets including experiments and wall-bounded flow models. Experimental data sets spanning a range of Reynolds numbers, with very long temporal and spatial domains, suggest that the rate of the observed temporal variations scales in inner units. The use of a convection velocity, uniform across heights, to transform space into time has a marginal effect on these features. Similarly, negligible effects are observed between internal and external geometries. Synthetic databases generated following the resolvent framework and the attached eddy model are employed to draw comparisons to the experimental databases. Our findings highlight the distinctive strengths of each: The broadband frequency input of the attached eddy model allows for a better statistical description as opposed to a narrow frequency input in the resolvent data sets; instantaneously, however, representative eddies are seen to lack some structural details leading to the observed temporal behavior, which is better replicated by resolvent modes. Overall, given the considerable variety of the input data tested, the agreement between the data sets highlights the robustness of the spatiotemporal characteristics of the examined UMZs. It also underpins the need for their proper inclusion in UMZ modeling from a statistical as well as an instantaneous viewpoint; the current analysis accentuates important performance indicators for both.

DOI: 10.1103/PhysRevFluids.7.104603

I. INTRODUCTION

The undeniable importance of wall-bounded turbulence has led to intense research efforts on the topic during the past several decades, providing us with a wealth of available data (both numerical and experimental). Its complexity has stimulated the development of a wide range of models, seeking some level of simplification of these flows. Currently, given the sheer range of data and adopted modeling approaches, comparisons are not necessarily straightforward, especially when diverse models are involved; they are, however, crucial in improving flow models and their robustness as well as in facilitating assessment of experimental data. In this paper, we present a comparison

*a.laskari@tudelft.nl

between two current prominent modeling approaches—one equation based (resolvent framework [1]), and one conceptual (attached eddy model, AEM [2])—as well as between time-resolved and snapshot particle image velocimetry (PIV) data. The comparisons will be limited to the streamwise velocity component, and in particular, the temporal characteristics of its instantaneous probability density function (PDF), as described in Ref. [3]: the overarching aim is to evaluate the robustness of these features in a wide variety of data.

Since the work of Meinhart and Adrian [4], the PDF of the instantaneous streamwise velocity has been increasingly scrutinized: local peaks in the PDF have been shown to indicate the presence of large zones of uniform momentum (UMZs) in the flow [5], delineated by thin regions of intense shear [6,7], reflected in the commonly observed staircaselike form of the instantaneous streamwise velocity profiles. From a structural perspective, these observations allowed connections with important notions of representative, energy-carrying, coherent structures populating the logarithmic and wake regions of wall-bounded flows [5], including large-scale motions (LSMs) and very-large-scale motions [8–11]).

More recently, UMZ characteristics have also been explored through the lens of drag reduction strategies [12,13]. In this context, a broad variety of input data has been employed to examine UMZs, including both experiments (PIV) and direct numerical simulations (DNS). Following the original experimental studies [4,5], the presence and characteristics of UMZs (as well as the intense-shear interfaces separating them) have been analyzed in experimental data of zero-pressure gradient (ZPG), incompressible, smooth [3,6,7,14–17] and rough [18] turbulent boundary layers (TBLs), TBLs subject to free-stream turbulence [19], TBLs in adverse pressure gradient (APG) [20,21], transonic, supersonic [20], and hypersonic [22] TBLs, in turbulent pipe flows [23] and atmospheric boundary layers [24,25]. Collectively, these works highlight the robustness and importance of these flow features. Of these studies, the majority employed high spatial resolution databases to assess specific structural elements, while only a few have explicitly examined temporal characteristics by employing stationary [3,16,20] and moving [17] time-resolved PIV. The main observations in this context were an increased temporal persistence of high-speed structures in the log region (involving a low number of UMZs [16]), as well as a presence of repeating patterns in the temporal evolution of the streamwise velocity PDF [3,17]. Recently, high resolution in both time and space domains has been available in DNS studies of ZPG and APG TBLs [26], as well as turbulent pipe flows [27,28], however, only a few studies (see Ref. [26]) explored the temporal persistence of UMZs specifically. They reported that high-speed structures are seen to persist for longer and are located closer to the free stream for ZPG flows, in line with experimental observations [16], while low-speed structures closer to the wall are more persistent in APG TBL flows [26]. One of the goals of this paper is to explicitly assess the importance of temporal information for the resulting characteristics of the streamwise velocity PDF and, in particular, the consequences of employing Taylor's hypothesis [29] for comparisons in the case of non-time-resolved data sets.

On the modeling side, there have been three distinct approaches that were specifically used to analyze UMZ development and characteristics, to date: the AEM [2], the resolvent framework [1], and the UMZ-vortical fissure model by Bautista *et al.* [30]. The first two were developed as conceptual and equation-based low-order flow representations, respectively. Their ability to reproduce key turbulent features and statistics guided subsequent fine-tuning [31] or input scale selection [32] during model development; resulting UMZ characteristics were then assessed as model outputs and compared with experimental observations. On the other hand, in the UMZ-vortical fissure model, the phenomenology of UMZs was used as model input while flow statistics were assessed as outputs to evaluate model performance [30]. Synthetic fields constructed using the AEM were able to reproduce the mean number of UMZs and its experimentally observed logarithmic scaling with Reynolds number; the model also underlined essential trends in the resulting population density and vertical extent of the associated structures [14]. Using the resolvent framework formulation, streamwise velocity fields of a representative LSM were able to reproduce UMZ behavior [15], while those composed of downstream traveling, single mode, and multimode hierarchies in the log region could reproduce experimentally observed temporal patterns of the streamwise velocity

TABLE I. Data-set details | $\mathcal{P}(U,t)$ construction details | symbol definition for each database

Dataset	Ref	Flow	Re_τ	$L_x \times L_y$	dx^+	$dx^+\|_{p.d.f.}$	$dt^+\|_{p.d.f.}$	$\mathcal{P}_{th}$	Line	Marker
SPIV1	[36]	TBL	2650	$11.6\delta \times 1.1\delta$	13	36	10.2	0.5	——	■
AEM	[31]	TBL	3200	$15.0\delta \times 1.3\delta$	32	32	9.7	0.5	-·-·-	▼
SPIV2	[39]	Channel	3900	$12.0\delta \times 1.0h$	29	29	10.1	0.5	——	■
SPIV3	[36]	TBL	5100	$11.9\delta \times 1.1\delta$	26	26	10.1	0.5	——	■
TRPIV	[16]	TBL	5300	$0.5\delta \times 1.2\delta$	27	27	10.4	0.5	- - -	□
R1	[1]	Channel	5300	$1.3h \times 1.0h$	27	27	10.4	3	·····	▽
SPIV4	[36]	TBL	7400	$11.6\delta \times 1.1\delta$	37	37	11	0.5	——	■
R2	[1]	Channel	15000	$0.5h \times 1.0h$	27	27	10.4	3	·····	▽

PDF; the latter two also allowed clear associations of the PDF behavior with the underlying velocity fluctuations [3]. On the other end, starting with instantaneous streamwise velocity profiles composed of randomly displaced vortical fissures of concentrated vorticity (satisfying a mean momentum equation analysis), statistics up to third (skewness) and fourth order (kurtosis) from high Reynolds number DNS studies could be replicated particularly well [30]; the fissure's thickness was seen to decrease with friction Reynolds number and the velocity jump across each fissure to scale with the friction velocity. These key observations further motivated the refinement of a conceptual model by Chini *et al.* [33] based on large-Reynolds number asymptotic analysis of the Navier-Stokes (NS) equations, which describes a 3D self-sustaining-process theory able to account for the formation and maintenance of UMZs with the aforementioned key attributes, in the inertial region of wall-bounded turbulent flows [34]. In this paper, we focus on the first two approaches, namely, the AEM and the resolvent framework; consistency of their background theoretical considerations has been previously examined [35], so here we are aiming to compare resulting flow representations and assess how well they match experimental observations. As mentioned above, the model output evaluated here is the PDF of the streamwise velocity and, in particular, its temporal evolution; as such, and given that the approaches discussed here are designed to successfully replicate a very wide range of flow behaviors, model (and experimental) data-set comparisons herein are meant to be targeted and not necessarily indicative of general model performance or applicability.

In what follows, the experimental and modeling data sets used in this paper will first be outlined. From a modeling perspective, the focus is entirely on structures anchored within the logarithmic region. Self-similarity imposes specific scaling relationships and allows for the most equitable comparison between the models (while the AEM contains exclusively self-similar eddies, the resolvent approach can include velocity modes throughout y—albeit with a higher degree of empiricism involved). The PDF construction and analysis described in Ref. [3] will subsequently be briefly outlined and expanded to account for the variety of input data employed in the present paper. These tools will then allow comparisons of the PDF behavior between data sets in the results section, as well as some more in-depth scrutiny of the previously observed patterns. Finally, some more in depth discussion and conclusions will follow.

II. DATA-SET DESCRIPTION

For the subsequent analysis, four different types of velocity fields are used: experimental velocity fields generated by time-resolved (TRPIV) and snapshot planar PIV (SPIV) and synthetic snapshots generated using the attached eddy model (AEM) and the resolvent framework (R). Both experimental and synthetic databases include data sets of internal (channel) and external (TBL) geometries and their details are provided in the sections below and outlined in Table I. Coordinates x, y, and z are used to denote the streamwise, wall-normal, and spanwise directions, respectively, and U, V, W the corresponding velocity components (lower case letters denoting fluctuations, following a Reynolds decomposition of the flow). Vectors are denoted with bold letters. Unless specified otherwise, all velocity components are in outer units, normalized using the free-stream velocity, U_∞ (or center-line velocity U_{CL} for internal geometries).

A. Time-resolved PIV (TRPIV)

The first experimental database contains a single data set of time-resolved planar PIV data from a TBL at $\mathrm{Re}_\tau = 5300$ in a streamwise–wall-normal plane [16]. The data set comprises 37 time-resolved runs, each containing 10 944 snapshots, covering about 14s of flow or 96 boundary layer turnover times (tU_∞/δ). Jones integral method was used to estimate δ, while u_τ was estimated employing the Clauser chart method [37] (similar results were obtained using the composite velocity profile by Chauhan *et al.* [38]). The field of view (FOV) is approximately $0.5\delta \times 1.8\delta$ in x and y, respectively. To minimize potential pixel-locking effects (especially pertaining to peak detection in the PDF of the velocity), filtering in time (effective time step of $dt = 0.027\delta/U_\infty$) and space (2D Gaussian filter with a 3×3 point kernel) was performed [14,39]. More details on the experimental setup can be found in Ref. [16].

It should be noted here that—given the variety of the databases included in this paper and our intent to assess the effects of using Taylor's hypothesis when comparing high- and low-speed data—we will consider this database as a baseline. It represents the full-scale problem when compared to the synthetic data sets and will not be modified when compared with the snapshot ones (all comparisons will be made in temporal units and as such only non-time-resolved data will be transformed by invoking Taylor's hypothesis).

B. Snapshot PIV: TBL (SPIV1, SPIV3, SPIV4)

A second planar PIV database of a TBL in streamwise–wall-normal planes, with an extended streamwise FOV ($L_x \approx 12\delta$), is also employed in this paper. Details of the data sets can be found in de Silva *et al.* [36]. To summarize, the database includes three non-time-resolved data sets, with 3000 independent velocity fields each, at three Reynolds numbers ($\mathrm{Re}_\tau = 2650, 5100, 7400$). To maintain spatial resolution while capturing a sufficiently large FOV to explore the large regions of coherence in the boundary layer, a multicamera arrangement is employed. Specifically, the experiments utilize an eight-camera array aligned in the streamwise direction to capture a FOV spanning $\sim 12\delta \times 1.1\delta$ in x and y, respectively. Each camera provides a spatial resolution of 4008×2672 pixels. The corresponding spatial resolution for each data set is summarized in Table I. Illumination is provided a Big Sky Nd-YAG double pulse laser that delivers 120 mJ/pulse. An in-house code is used for processing the PIV image-pairs [40]. δ and u_τ are computed by applying the composite velocity profile of Chauhan *et al.* [38].

C. Snapshot PIV: Channel (SPIV2)

A third planar PIV database of a channel in streamwise–wall-normal planes, with an extended streamwise FOV ($L_x \approx 12\delta$), is also employed for completeness. Details of the dataset can be found in Kwon *et al.* [39]. To summarize, the database includes one non-time resolved data set, with 590 independent velocity fields, at an intermediate Reynolds number of $\mathrm{Re}_\tau = 3900$. To maintain spatial resolution (see Table I), while capturing a sufficiently large FOV to explore the large regions of coherence in the boundary layer, a multi-camera arrangement is employed. Specifically, the experiments utilize a four camera array (each providing a spatial resolution of 4008×2672 pixels) aligned in the streamwise direction to capture a FOV spanning $\sim 12\delta \times 2h$ in x and y, respectively, although only the lower half of the channel was used in subsequent calculations.

D. Resolvent framework (R1, R2)

The synthetic database generated using the resolvent framework contains two data sets of turbulent channel flow at two different Reynolds numbers, henceforth referred to as R1 ($\mathrm{Re}_\tau = 5300$) and R2 ($\mathrm{Re}_\tau = 15\,000$). Each data set contains 21 time-resolved runs, each containing 1300 snapshots of instantaneous streamwise velocity fields. Brief outlines of the resolvent framework and of the construction details of these snapshots are included here for completeness; for more details, the reader is referred to Refs. [3,41], respectively.

The resolvent framework formulation for wall-bounded flows [1] treats the NS equations as an input-output system: the nonlinear term $\boldsymbol{f_k}$, acts as an intrinsic forcing, exciting the linear NS operator (the resolvent) $\boldsymbol{\mathcal{H}_k}$, following a Fourier transform in the homogeneous directions in space and in time, with $\boldsymbol{k} = (k_x, k_z, \omega)$ denoting the wave number/frequency triplet. The corresponding output response from this forcing, $\boldsymbol{u_k}$, comprises downstream propagating traveling waves and represents, in the Fourier domain, the velocity fluctuations around a wall-varying mean profile $U(y)$ based on a Reynolds decomposition of the flow. The linear operator requires only knowledge of $U(y)$ for its construction and, following a singular value decomposition, can be formulated in terms of left ($\psi_{\boldsymbol{k},j}$) and right ($\phi^*_{\boldsymbol{k},j}$) singular functions and singular values ($\sigma_{\boldsymbol{k},j}$) for each $\boldsymbol{k}$:

$$\mathcal{H}_{\boldsymbol{k}} = \sum_{j=1}^{\infty} \psi_{\boldsymbol{k},j} \sigma_{\boldsymbol{k},j} \phi^*_{\boldsymbol{k},j}. \tag{1}$$

The velocity response can then be approximated as a weighted sum of resolvent modes [41],

$$\boldsymbol{u_k} = \sum_{j=1}^{\infty} \sigma_{\boldsymbol{k},j} \psi_{\boldsymbol{k},j} \overline{\chi}_{\boldsymbol{k},j} = \sum_{j=1}^{\infty} \psi_{\boldsymbol{k},j} \chi_{\boldsymbol{k},j}, \tag{2}$$

where the weights $\overline{\chi}_{\boldsymbol{k},j}$ are the coefficients of projection of the true nonlinear forcing $\boldsymbol{f_k}$ onto the forcing modes, and $\chi_{\boldsymbol{k},j} = \sigma_{\boldsymbol{k},j} \overline{\chi}_{\boldsymbol{k},j}$. The resolvent operator has been shown to be low rank for those wave-number triplets corresponding to important features of wall-bounded turbulence [41] and, in what follows, a rank-1 approximation will be adopted and the singular value subscript j will be dropped for clarity: $\boldsymbol{u_k} = \psi_{\boldsymbol{k}} \chi_{\boldsymbol{k}}$.

To construct the data sets discussed above, an appropriate selection of key wave-number triplets is required; for each resulting response mode, the corresponding projection weight $\chi_{\boldsymbol{k}}$ is subsequently chosen and the full fluctuating velocity contribution is then superimposed on the known mean profile. For the two data sets included here, the discrete wave-number/frequency input selection is guided on one hand by the need to include representative log region structures while allowing enough complexity to break the purely periodic nature of the model and, on the other, by a wish to retain as much simplicity as possible. Given those constraints, the data sets are constructed using three self-similar hierarchies localized in the log region and comprising five (six) triadically consistent members each, in the case of R1 (R2). With respect to the modes' wall-normal location, the shortest member of each hierarchy is centered at the start of the inertial region in the mean velocity profile, $y_{c,5}/h = 3/\sqrt{Re_\tau} = 0.0046$ ($y_{c,6}/h = 0.0245$) [42], and defines the location of all other members in the hierarchy through $y_{c,m} = A^{5-m} y_{c,5}$ ($y_{c,m} = A^{6-m} y_{c,6}$) for R1 (R2). The longest member in each hierarchy is constrained by $y_{c,1}/h \leqslant 0.4$, thus prescribing the total number of members, while A is chosen equal to the golden ratio, $\phi = 1.6$. With respect to the modes' wave-number content, we select the wavelength of the largest mode in one of the hierarchies to be representative of an LSM, with $k_{x1} = 1.8$ ($k_{x1} = 2$) for R1 (R2). Its corresponding spanwise wave number k_{z1} is chosen such that, given the scaling relationships $\lambda_z \sim y_c$ and $\lambda_x \sim y_c^2$, the aspect ratio condition ($\gamma = k_z/k_x \gg 1$) is satisfied throughout the rest of the hierarchy [43]. The wave numbers of the outmost modes in the other two hierarchies are selected to be triadically consistent, while being noninteger multiples of each other; geometric self-similarity then dictates the wave numbers for the rest of the modes and their convection velocity is prescribed by their wall normal location: $c_m = \overline{U}(y_{c,m})$. Finally, given the choice of wave-number/frequency triplets, the projection weights for the resulting response modes are selected separately and chosen such that the resulting fluctuation intensity (u_k^2) decreases logarithmically with y.

E. Attached eddy model (AEM)

A synthetic data set generated following the AEM is included in the analysis. The database is set up following the configuration published in Eich *et al.* [31]. To summarize, the AEM flow

fields are computed based on a packet of Λ eddies, which has been shown to both statistically [44] and structurally represent a TBL [14]. A set of vortex rods that contain a Gaussian distribution of vorticity about its core are used to construct the representative eddies. To compute the flow field, Biot-Savart calculations are performed over the vortex rods. This process is then repeated for each hierarchy of representative eddies in the field, here chosen to be six, which corresponds to a flow field at $\mathrm{Re}_\tau = 3200$. The domain size was chosen such the maximum of the Reynolds shear stress is one and $\kappa \approx 0.4$ [14].

III. PDF CONSTRUCTION

The PDF of the streamwise velocity, $\mathcal{P}(U)$, is constructed using instantaneous velocity vectors from either consecutive snapshots within time-resolved runs [TRPIV, R1, R2, Fig. 1(b)] or from spatially overlapping regions of independent, non-time-resolved snapshots [SPIV1, SPIV2, SPIV3, SPIV4, AEM, Fig. 1(a)]. For the latter, the long streamwise extent available allows the snapshots to be divided in equidistant regions, for each of which a PDF is computed [solid black outlines and sharp contours in Fig. 1(a)]. Spatial (and temporal) coherence is then provided by the PDFs of consecutive overlapping regions in x [dashed outlines in Fig. 1(a)] with increasing x indicating previous time instances. This overlap is chosen such that, assuming a single, uniform convection velocity, the resulting temporal resolution of the PDFs is comparable between the snapshot and time-resolved data sets. It should be noted here that temporal resolution is matched in inner units ($dt^+|_{\mathrm{PDF}}$ in Table I), which allows for a better scaling analysis for the range of Reynolds numbers included, making this the only difference from the analysis described in Ref. [3]. This is further ensured by the choice of convection velocity used to transform space to time ($U_c = 0.81U_\infty$), primarily chosen to correspond to the convection of a representative large-scale structure (see, for example, Ref. [45]). One of the goals of the present paper is to identify to which extent such an assumption affects the resulting PDF behavior. For the AEM, it should also be noted that employing a wall-normal varying convection velocity (and periodic boundary conditions), as well as incorporating spanwise meandering, as described in Eich *et al.* [31], only led to marginal changes in the metrics presented here, while the overall trends remained the same. Constraints for the construction of the PDF are imposed in both x and y in all data sets. With respect to x, the streamwise extent used to construct the PDF is chosen such that the observed modal peaks in the PDF are well-converged, without averaging out of the smallest modal peaks present in each frame. Following Ref. [14], an optimal streamwise extent of $\mathcal{L}_x^+|_{\mathrm{PDF}} = 2000$, is chosen for all data sets. In the wall-normal direction, all velocity vectors within the turbulent region are included; we only exclude those belonging in the irrotational free stream (quiescent core) in external (internal) geometries. For consistency and simplicity, the turbulent/nonturbulent interface is identified using the isocontour lines of $U = 0.95U_\infty$ for all data sets, following Ref. [39]. We note that the use of other methods such as a kinetic energy threshold [46] for the two experimental databases did not alter any of the results or conclusions presented herein. It did, however, afford, a smoother free-stream identification for the TRPIV data set compared to the abrupt drop of the high PDF values seen here [Figs. 2 and 6(a)], likely due to increased free-stream turbulence levels present in that flow (see also the relevant discussion in Ref. [16]). Similar to the temporal resolution requirements discussed above, comparable spatial resolution (in wall units) for the PDF construction is also ensured between data sets ($dx^+|_{\mathrm{PDF}}$ in Table I) by undersampling the lower Reynolds number ones. The vectors contained within these limits are then distributed in 67 bins for $U \in [0, U_\infty]$ (of size approximately $0.4 \pm 0.04U_\tau$).

The resulting $\mathcal{P}(U, t)$ reveal interesting visual differences depending on the chosen scaling, the Reynolds number of each data set, as well as the data-set type (experimental or synthetic). Regarding experimental data sets, the use of a uniform convection velocity does not seem to affect the resulting PDF patterns, while the temporal data set (TRPIV) is seen to result in slightly more noisy fields (Fig. 2). It should be noted here that, these temporal patterns in $\mathcal{P}(U, t)$ are discussed on the basis of variations in $U_*(t)$: $U_* = \min(U|\mathcal{P}(U, t) > \mathcal{P}_{\mathrm{th}})$ (see Fig. 3), following the procedure

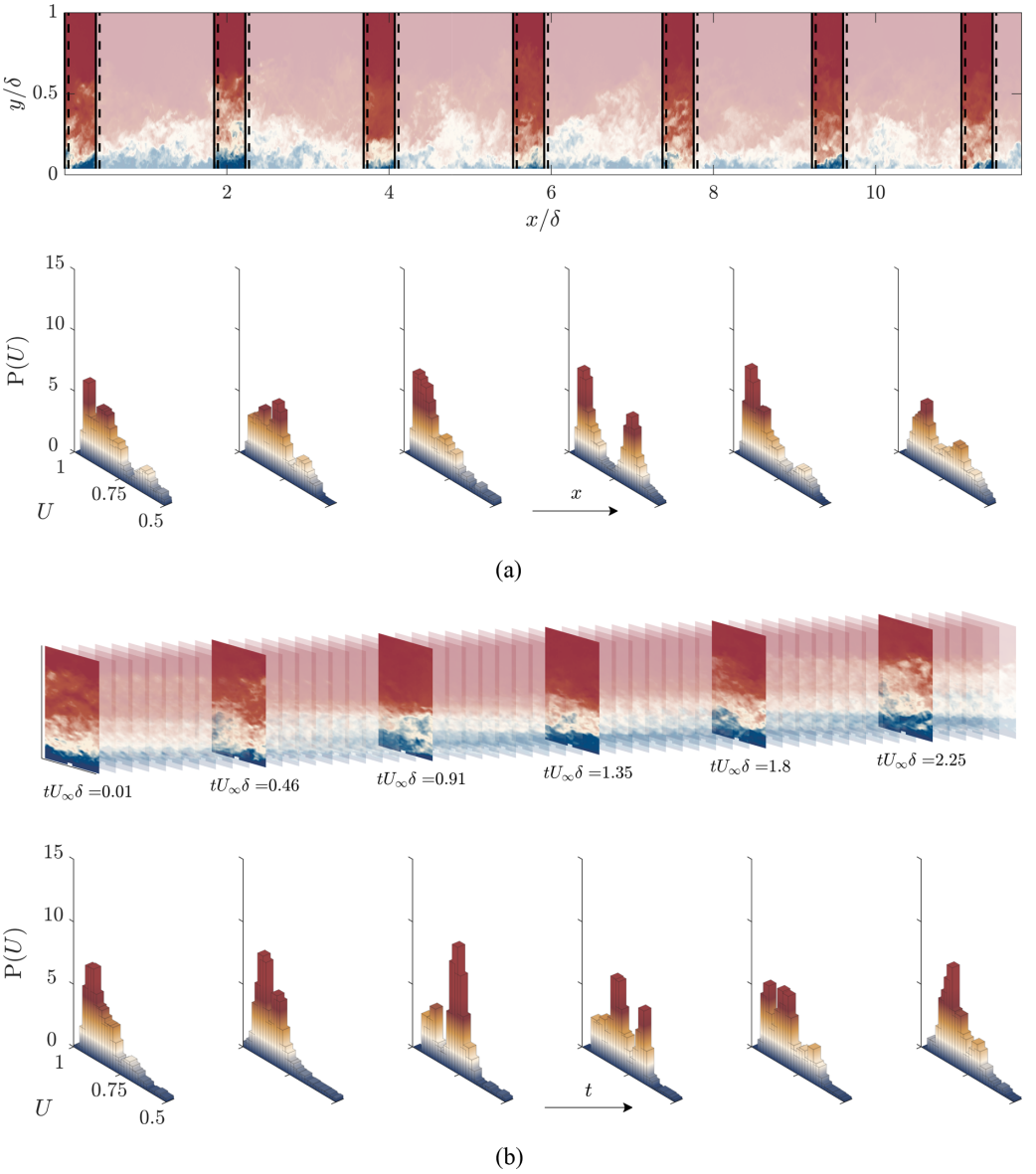

FIG. 1. Construction of $\mathcal{P}(U,t)$: (a) Spatial data (SPIV1, SPIV2, SPIV3, SPIV4, AEM), (b) temporal data (TRPIV, R1, R2). In (a), the full spatial extent, L_x, is divided into regions of $\mathcal{L}_x^+|_{\mathrm{PDF}} = 2000$, while the same extent is selected from the time-resolved snapshots in (b). To match the temporal resolution in (b), an appropriate level of spatial overlap is used for each consecutive region in (a) (indicated with dashed lines) when constructing the PDF, while also assuming a constant $U_c = 0.81$.

proposed in Ref. [3]. We are particularly interested in the temporal rate of transitions in U_*, defined as the angle $\phi = \tan^{-1}(\Delta U_*/\Delta t)$. The threshold $\mathcal{P}_{\mathrm{th}}$ used for each of the data sets can be found in Table I and for further details on how that choice influences the analysis, the reader is referred to the relevant discussion in Ref. [3]. Returning to the data-set comparison (Fig. 2), the above defined rate of transitions is seen to increase with Reynolds number when scaled in outer units, while better agreement is observed when the temporal extent is matched in wall units. With respect to the data-set

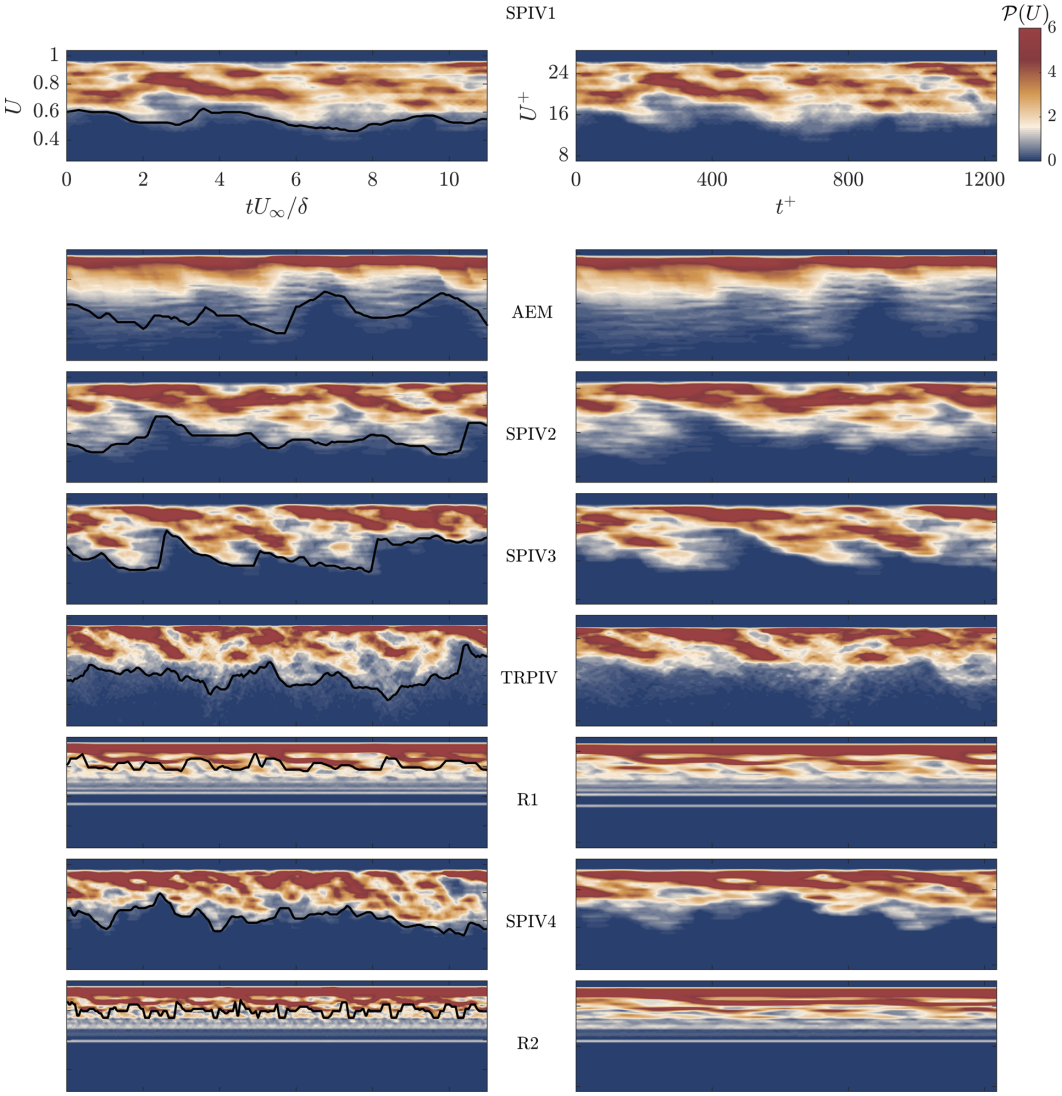

FIG. 2. Variation of $\mathcal{P}(U)$ over time in increasing Re_τ from top to bottom. Matching temporal extent in outer (left) and inner (right) units. Black solid lines denote $U_* = \min(U|\mathcal{P}(U,t) > \mathcal{P}_{\mathrm{th}}$.

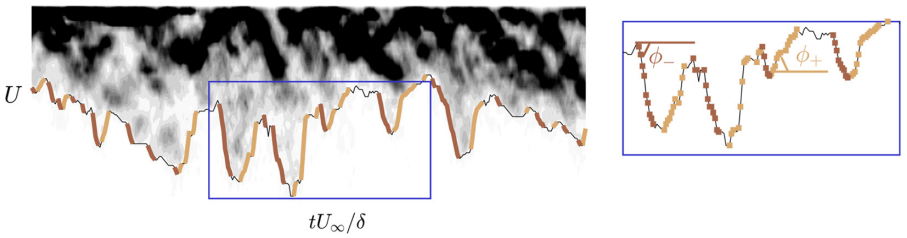

FIG. 3. An illustration of the transitions in $\mathcal{P}(U,t)$–TRPIV, adapted from Ref. [3]. The identified ϕ_+ ($\Delta U_* > 0$, light colors) and ϕ_- ($\Delta U_* < 0$, dark colors) transitions of U_* are shown on the left, with the corresponding definitions on the detail on the right.

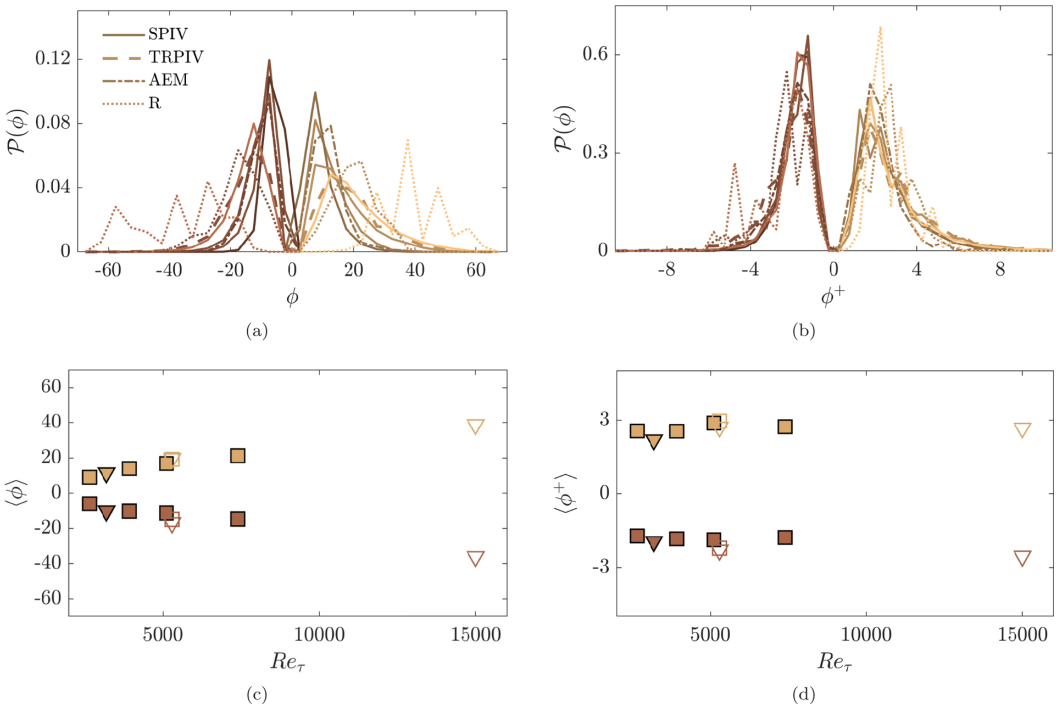

FIG. 4. Probability density function and mean values of transition angles ϕ_+ and ϕ_-, in outer (a), (c) and inner (b), (d) scaling ($\phi = \tan^{-1}(\Delta U_*/\Delta t)$). SPIV is denoted by ■, AEM by ▼, TRPIV by □, and R1 (R2) by ▽ (see also Table I). Colors of each transition angle as in Fig. 3 (with lighter shades indicating increasing Re_τ).

type, and before moving forward with a quantitative analysis of these features, from a purely visual inspection, the two synthetic databases are able to reconstruct different aspects of the experimental patterns. The AEM data set, given its broadband frequency input, allows some level of variation in $\mathcal{P}(U,t)$ for a larger range of velocities compared to the resolvent framework data sets which contain a preselected set of scales (particularly notable for velocities $<0.6U_\infty$). However, the largest $\mathcal{P}(U,t)$ values are confined to a very narrow range around $0.95U_\infty$ for the AEM and, although some transitions to lower velocities are still observable and comparable in rate with the experimental data sets, they are much less discernible. In contrast, the patterns from the two resolvent data sets are more clearly formed and are also seen to qualitatively support the aforementioned Reynolds number variation in terms of their temporal extent. These differences between the models, which will be analyzed in more detail in the next sections, essentially reflect the relative lack of frequency content for the chosen resolvent data sets and an incomplete instantaneous spatial/temporal organization for the AEM.

In the quantitative analysis that follows, statistics of the angles ϕ describing the transitions in $\mathcal{P}(U,t)$ are compared first, in all the available data sets, with ϕ_+ indicating transitions to higher velocities with increasing time ($\Delta U_* > 0$) and ϕ_- transitions to lower ones ($\Delta U_* < 0$).

IV. RESULTS

A. Rate of temporal transitions

Both the PDF and the mean values of the transition angles exhibit fairly good collapse in inner units for all data sets, especially for ϕ_- [Figs. 4(b) and 4(d)], while a monotonic increase in both angles is seen with Reynolds number in outer units [Figs. 4(a) and 4(c)], in line with the earlier

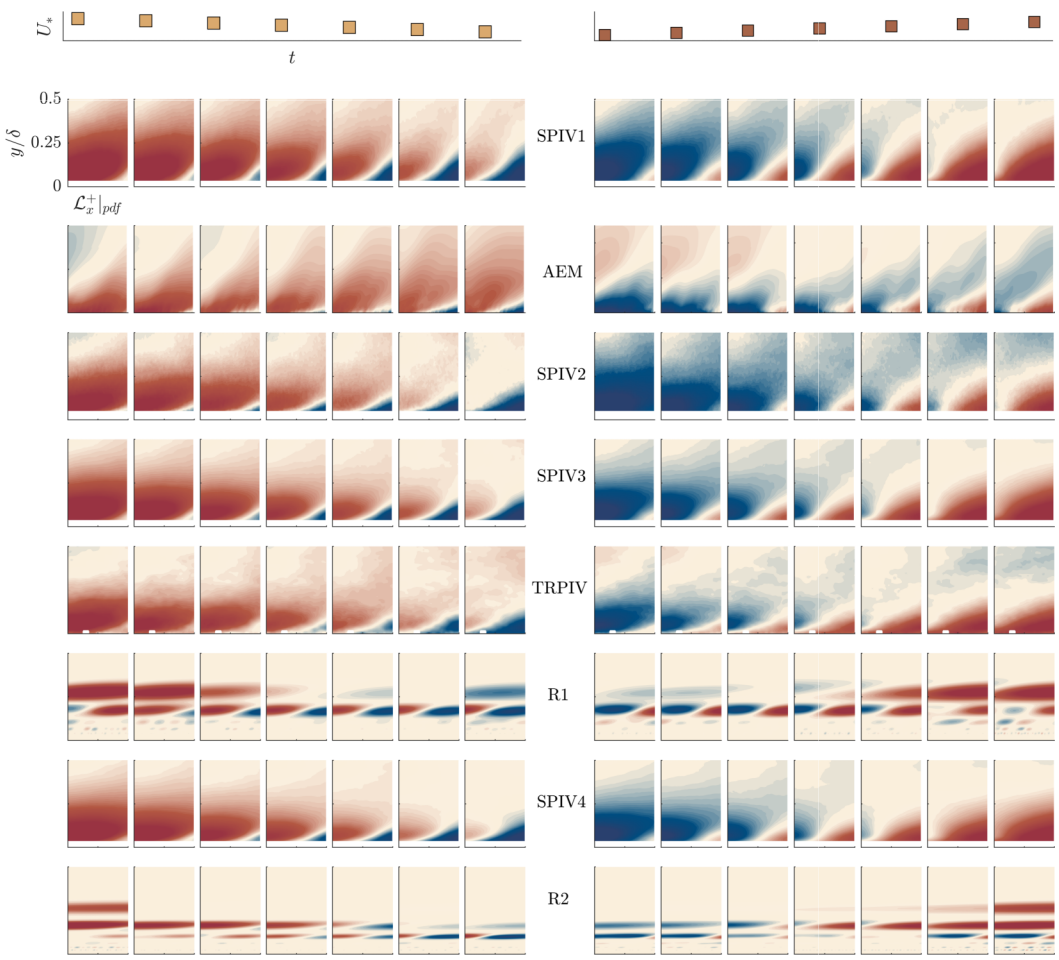

FIG. 5. Conditionally averaged streamwise velocity fluctuations in increasing Re_τ (from top to bottom) for each type of transition, $u|\phi_+$ (left) and $u|\phi_-$ (right) as shown schematically with symbols on top (to provide spatially continuous structures from left to right in the contour plots, time increases from right to left for the indicated transitions in U_*, following the convention from Ref. [3]).

observations from the $\mathcal{P}(U,t)$ fields (Fig. 2). In particular, results from all experimental data sets indicate a very good collapse for both ϕ_- and ϕ_+ angles in inner units. The resolvent-based data sets (R1, R2) indicate a more discrete range of values for the transition angles (especially noticeable in outer normalization) due to the model's discrete scale input. On the other hand, the AEM data set, being broadband in frequency space, allows for a fuller range of the resulting transitional angles, with only ϕ_+ being slightly underestimated due to a narrower tail of the PDF [Fig. 4(b)]. Overall, given the broad range of the input data used here, these metrics illustrate the robustness of the observed patterns despite these discrepancies.

It has been previously shown that the transitions in the PDF of U discussed above were associated with well-defined variations in the fluctuations, revealed through conditional averaging [3]. More precisely, ϕ^+ transitions (toward higher velocities) were shown to be associated with the passage of an inclined low-speed structure followed by a high-speed one (Fig. 5, left), while the opposite was true for ϕ^- transitions (Fig. 5, right). Very similar behavior in the conditionally averaged fluctuation fields was observed in the current study for all additional data sets. Regarding the experimental data

sets, the use of a uniform convection velocity did not seem to affect the resulting structures in either the phase or the amplitude of the observed patterns. For similar Reynolds numbers (SPIV3, TRPIV), their inclination with respect to the horizontal as well as their vertical extent also compare very well, however, they do seem to decrease with increasing Reynolds number (SPIV1, SPIV4). The PDF threshold $\mathcal{P}_{\text{th}}$ has been shown to affect the wall normal location where the structures are centered and, to some degree, their vertical extent and inclination [3]; here, the same threshold is applied to all experimental data sets for consistency (see Table I), however, higher PDF values for lower velocities are observed in general for higher Reynolds number data sets (see Fig. 2). As such, the choice of a constant $\mathcal{P}_{\text{th}}$ for all data sets might be partly responsible for these differences with the Reynolds number. On the other hand, for modeled data sets there are much more pronounced disparities. As was already discussed in our previous work [3], the resolvent data sets are able to replicate the phase change in the conditional structures observed in experiments, however, they are very localized in y due to the discrete frequency input of the model. On the contrary, the AEM, given its broadband frequency input, succeeds better in capturing a wider wall-normal extent for the conditional fluctuating fields, however, the phase and, to a smaller extent, the geometry of the structures exhibit differences from all other data sets. This is intriguing, given the success of the model in statistically predicting the rate of these transitions (see Fig. 4). It is likely that the reason for this discrepancy lies in the lack of clearly formed patterns in the PDF for the AEM, where there is an almost monotonic decrease in the PDF values with velocity (Fig. 2). Tracing the transitions of $U_* = \min(U|\mathcal{P}(U,t) > \mathcal{P}_{\text{th}})$ in those cases might lead to correct overall transition rate estimates but a mismatch in where these transitions occur in time, resulting in discrepancies when fluctuating fields are then averaged over these snapshots. Overall, the robustness of these features is clearly highlighted when assessing both snapshot and time-resolved PIV data, while the differences observed in the models appears to be mostly from their own distinct inherent limitations.

B. Temporal coherence

As was mentioned above, the local peaks of $\mathcal{P}(U)$ are indicative of the presence of UMZs in the flow at a specific snapshot (see, for example, Fig. 1), a method that has been followed almost universally for UMZ identification and statistical analysis of their characteristics (one notable exception been the method described in Ref. [47]). When longer time (space) information is available, the resulting $\mathcal{P}(U,t)$ exhibits robust temporal patterns (Fig. 2), the rate of which was quantified in the first part of this section. These transitions have also been indirectly linked to the temporal variation in the number of UMZs (see the relevant discussion in Ref. [3]). Aside from these transitions, however, time (space) information allows further analysis of UMZ characteristics more directly. In particular, visual inspection of $\mathcal{P}(U,t)$ reveals that an increase in Reynolds number in outer scaling leads to a decrease in the temporal coherence of local PDF peaks (Fig. 2, left), an observation also reflected in the resolvent data sets. On the other hand, temporal coherence of UMZs is much less discernible in the AEM, where there is an almost monotonic decrease in the values of $\mathcal{P}(U,t)$ for decreasing velocity [especially obvious in the 3D representation of the morphology in Fig. 6(d)]. The topic of temporal coherence has been partly addressed by Laskari *et al.* [16] who observed that high-speed events, linked to a low number of UMZs, exhibited longer coherence than low-speed ones, associated with multiple UMZs. In this paper, we follow a more targeted approach, seeking to quantify the temporal coherence of UMZs for selected modal velocities, focusing on Reynolds number scaling and individual model performance.

In all data sets, UMZs are identified as local peaks of $\mathcal{P}(U)$ for each snapshot (see also Fig. 1); the detection parameters are kept the same with some appropriate adjustments made for the modeling databases due to their bias toward velocities closer to U_∞, which lead to higher maximum PDF values (also reflected in the choice of $\mathcal{P}_{\text{th}}$, Table I). For a relevant discussion on this disparity see Ref. [3], and for more details on the detection thresholds see Ref. [16]. Only peaks identified in at least three consecutive snapshots ($t \sim 20^+$) are considered. The number of consecutive snapshots for which a UMZ can be detected has previously been used as an indication of temporal coherence

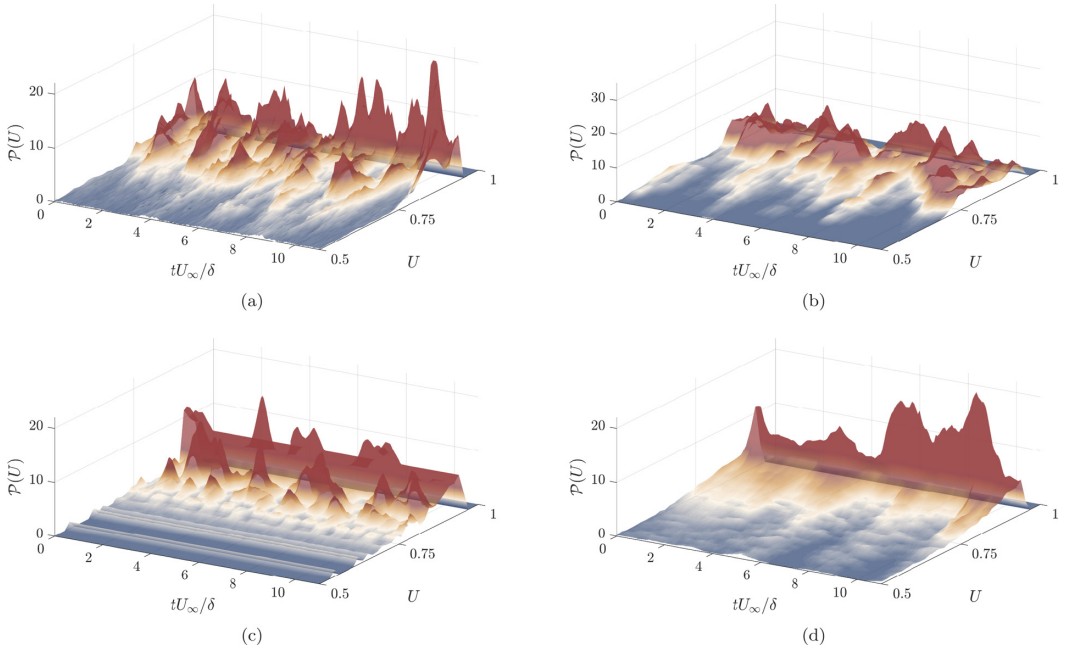

FIG. 6. 3D variation of $\mathcal{P}(U, t)$ for experimental (top) and model datasets (bottom): TRPIV (a), SPIV3 (b), R1 (c), AEM (d).

[16]. To avoid the discrete nature of this approach, here we introduce a different metric, based on the 3D peak morphology that also exploits the available temporal information more fully. Specifically, the temporal extent, $\mathcal{T}(U_m)$, of the time-coherent UMZ at a modal velocity U_m, is defined as the time for which the peak retains at least 85% of its maximum value (see Fig. 7 for an illustration of the approach). The total drop-off percentage of the maximum peak value varies significantly between peaks of different data sets and can be much greater than 85%; this threshold percentage,

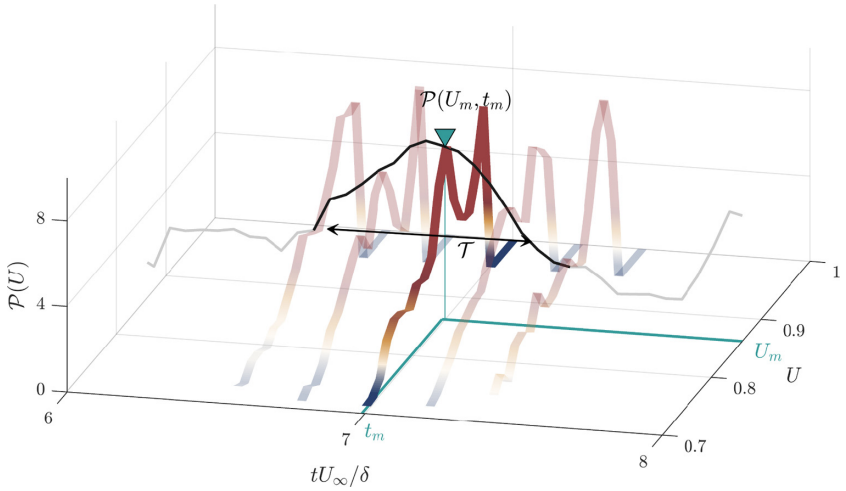

FIG. 7. Illustration of the evolution of $\mathcal{P}(U_m, t_m)$ (symbol), an instantaneous, time-coherent UMZ peak at time t_m and modal velocity U_m, and its extent in time, $\mathcal{T}$, calculated at 85% of the peak value.

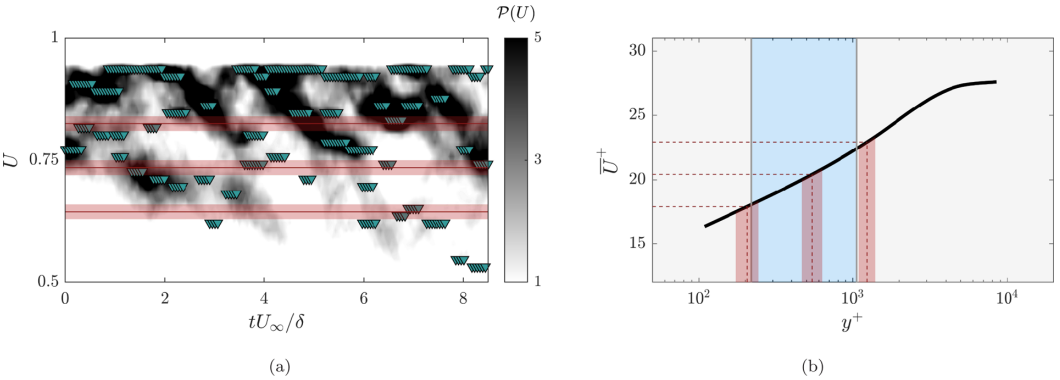

FIG. 8. (a) Illustration of multiple time-coherent UMZ peaks (symbols) overlaid on $\mathcal{P}_U$. Statistics of $\mathcal{T}(U_m)$ in what follows are calculated at $0.63 \leqslant U_m/U_\infty \leqslant 0.66$, $0.72 \leqslant U_m/U_\infty \leqslant 0.75$, and $0.81 \leqslant U_m/U_\infty \leqslant 0.84$ (shaded regions). (b) Corresponding wall-normal locations for the selected velocity regions in (b), based on the mean, $\overline{U}$ (here for TRPIV). Blue shaded region indicates the logarithmic region extent $(3/\sqrt{\mathrm{Re}_\tau} \leqslant y/\delta \leqslant 0.2)$.

however, (identical for all data sets for consistency) is chosen because all identified peaks decrease monotonically to at least 85% of their original value. As such, here we are interested in comparing the time it takes for peaks to reach this threshold rather than the final drop-off level of their maximum value. This definition of time coherence explicitly combines space and time information: at time t_m, a spatial extent $\mathcal{L}_x^+|_{\mathrm{PDF}} = 2000$ is used to construct $\mathcal{P}(U, t_m)$ and identify $\mathcal{P}(U_m, t_m)$ as a local peak at a modal velocity U_m; the peak's extent in time, $\mathcal{T}(U_m)$, is then determined by the peak morphology in the temporal axis. It follows that statistical analysis of the temporal coherence can be performed for each modal velocity U_m, according to the binning procedure followed for the construction of $\mathcal{P}$ (see Sec. III). To improve convergence, however, since the resulting temporal coherence does not vary significantly with U_m, the statistical analysis for $\mathcal{T}(U_m)$ is performed in bins of double the size $[0.03U_\infty$, red shaded regions in Fig. 8(a)].

In what follows, we analyze the temporal coherence of modal velocity peaks belonging in three representative bins which correspond (based on the mean velocity profile) to wall-normal locations in the middle of the log region $(3/\sqrt{\mathrm{Re}_\tau} \leqslant y/\delta \leqslant 0.2)$, as well as close to its lower and upper limits [see Fig. 8(b)]. It should also be noted that for all subsequent results, a temporal filter (effective resolution of $dt^+ = 32$) was applied to all data sets. The scaling trends discussed below remained largely unchanged; filtering mostly affected the time-resolved experimental data set (TRPIV) for which $\mathcal{P}(U)$ was more noisy (see also Fig. 2) and exhibited slightly lower values of temporal coherence than all the rest. The filter size was selected such that the resulting temporal resolution would be comparable to the spatial one (see Table I) and was the minimum above which the relative values of $\mathcal{T}$ between data sets remained unchanged.

The conditionally averaged PDF values, preceding and following the identified UMZ peaks in time, indicate that for all data sets, similar to the PDF transition rates, ϕ_- and ϕ_+, inner scaling is successful in collapsing the resulting peak shapes—as far as their extent in time is considered (see Fig. 9, right). As was mentioned earlier, however, the average level of drop-off of the maximum peak value varies markedly between data sets without an apparent trend with respect to Reynolds number scaling. It is interesting to note that time-resolved data sets (TRPIV, R1, and R2) mostly exhibit higher drop-offs compared to the rest, especially for higher velocities, although the source of this behavior is likely different for the two databases. For the synthetic data sets based on the resolvent framework (R1, R2), the higher level of drop-off in well-defined peaks can be attributed to the discrete scale input of the model: superposition of selected modes creates distinct modal peaks in an otherwise monotonically varying PDF of the mean velocity. The sole exception to this trend, in the data shown here, is data set R1 for $0.72 \leqslant U_m/U_\infty \leqslant 0.75$ [dotted lines in Figs. 9(c)

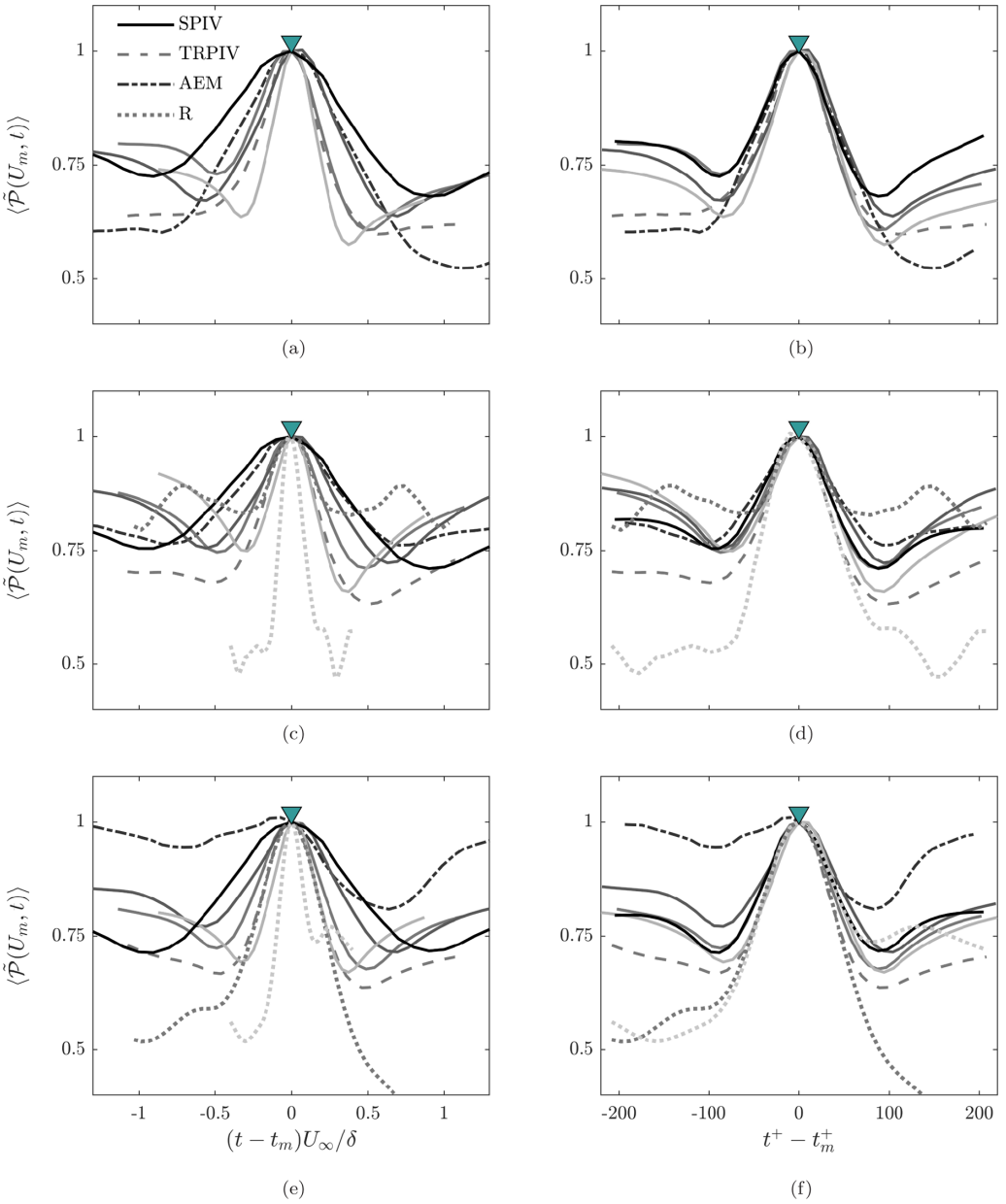

FIG. 9. Conditionally averaged PDF values with respect to time, $\langle\tilde{\mathcal{P}}(U_m,t)\rangle$, for all data sets, normalised with the maximum peak value, $\mathcal{P}(U_m,t_m)$. Temporal axis in outer (left) and inner (right) scaling, for $0.63 \leqslant U_m/U_\infty \leqslant 0.66$ (a), (b); $0.72 \leqslant U_m/U_\infty \leqslant 0.75$ (c), (d); and $0.81 \leqslant U_m/U_\infty \leqslant 0.84$ (e), (f). Increasing Re_τ is denoted with lighter colors. Following Fig. 8(a), symbols denote the UMZ peaks at $t = 0$.

and 9(d)]; for both R1 and R2 data sets, however, this velocity range is at the lower edge, above which $\mathcal{P}(U,t)$ varies significantly (see also Fig. 2) and as such not as indicative or statistically accurate. This confinement of significant PDF values in a limited velocity range is one of the main limitations of the two resolvent-based data sets and is also apparent in the lack of any peaks present at the lowest velocity range [$0.63 \leqslant U_m/U_\infty \leqslant 0.66$, Figs. 9(a) and 9(b)]. On the other hand, the

high average drop-off level observed in the time-resolved experimental data set (TRPIV) when compared to almost all other non-time-resolved ones (SPIV1, SPIV2, SPIV3, SPIV4, solid lines in Fig. 9), regardless of Reynolds number, might be more indicative of differences due to space-time conversion—a process which was not observed to impose any significant influence on the metrics discussed up until this point. As mentioned in Sec. III, the time-resolved data set did exhibit overall higher $\mathcal{P}(U)$ values compared to its snapshot counterpart at comparable Reynolds numbers [Figs. 2, 6(a), and 6(b)], attributed to the higher free-stream noise present; however, given the normalization of the peak magnitude here (the drop-off is quantified relative to the maximum peak value), this is not likely to influence the observed disparity between low- and high-speed data sets. Finally, the AEM data set (dot-dash lines in Fig. 9) exhibits progressively worse collapse of the conditional peak shape with increasing velocity, with larger temporal coherence and very low drop-off levels, compared to the rest of the data sets.

These findings follow directly from the considerable disparity observed in the $\mathcal{P}(U,t)$ contours of the data set [Figs. 2 and 6(d)], where the temporal patterns of the PDF were broader and less prominent. The relative lack of instantaneous information in the construction of the AEM dataset (eddies randomly placed in the spatial domain) can partly explain these deviations from the experimentally observed behavior. Another likely culprit of such discrepancies, however, is the much larger number of vectors representative of higher velocities (as U_∞ is approached) relative to the other data sets, inherent in the construction of the AEM: packets of nested eddies superimposed on an otherwise irrotational frees tream and inducing a corresponding superposition of velocity deficits, lead to a much denser eddy population closer to the wall than closer to the free stream. As such, the largest eddies (with the lowest velocity deficits) occupy an increasingly large proportion of the flow field, which is then characterized by velocities close to U_∞ and leads to the aforementioned almost monotonic increase of $\mathcal{P}(U,t)$ with increasing velocity.

Looking more closely at the statistics of the temporal coherence, $\mathcal{T}$, the same Reynolds number scaling for inner and outer normalization as the one observed for the conditionally averaged peak shape is also observed here (Figs. 10 and 11). More specifically, the PDF of $\mathcal{T}(U_m)$ for all experimental data sets and all three representative velocity regions for U_m collapses in inner units (Fig. 10, right). Due to the aforementioned limitation in the two lowest velocity ranges for R1 and R2, it is only for the highest velocity band [$0.81 \leqslant U_m/U_\infty \leqslant 0.84$, Fig. 10(f)] that the two resolvent-based data sets also collapse on the experimental ones, while the lack of statistical convergence is clear for $0.72 \leqslant U_m/U_\infty \leqslant 0.75$ [Fig. 10(d)], and the lack of any peaks present at lower velocities can be seen for $0.63 \leqslant U_m/U_\infty \leqslant 0.66$ [Fig. 10(b)]. On the other hand, the PDF of $\mathcal{T}(U_m)$ based on the AEM data set is seen to deviate from all other data sets and for all three U_m regions, leaning toward higher values on average and a slightly more limited range overall. The latter is an interesting contrast to the broader shape of $\mathcal{P}(\mathcal{T}^+)$ for the R1 and R2 data sets (at the highest velocity range). A limited frequency content in the construction of the resolvent data sets was seen to be reflected in a limited range for the PDF transitions (ϕ_+ and ϕ_-) when compared to the wider range of values from the broadband frequency content in AEM (Fig. 4); however, the relative lack of temporal information on the latter that is inherently present in the former leads to the opposite picture emerging for the two databases in the PDF of temporal coherence.

These observations are further supported in the scaling of the mean values of $\mathcal{T}$ which, for most data sets, is seen to approximate a value of $\langle \mathcal{T}^+ \rangle = 100 \pm 50$ (Fig. 11, right). Values for R1 and R2 are seen to deviate slightly from this when $0.72 \leqslant U_m/U_\infty \leqslant 0.75$ and no data is available for $0.63 \leqslant U_m/U_\infty \leqslant 0.66$. In contrast, for the AEM, agreement is only found for this lowest velocity range while higher values of $\langle \mathcal{T}^+ \rangle \approx 130$ are predicted for the higher velocities. In line with the observations for $\mathcal{P}(\mathcal{T})$, Reynolds number scaling for $\mathcal{T}$ is also reflected in the standard deviation around the mean (error bars in Fig. 11), which is seen to decrease with Reynolds number in outer units (Fig. 11, left), while it is almost constant for all data sets ($\sim 50^+$) in inner scaling. These trends also delineate more clearly the improved predictions for R1 and R2 in the highest velocity range (indicated by a collapse with the experimental estimate of the standard deviation around $\langle \mathcal{T} \rangle$ for $0.81 \leqslant U_m/U_\infty \leqslant 0.84$). With respect to the experimental data sets, it should be noted that,

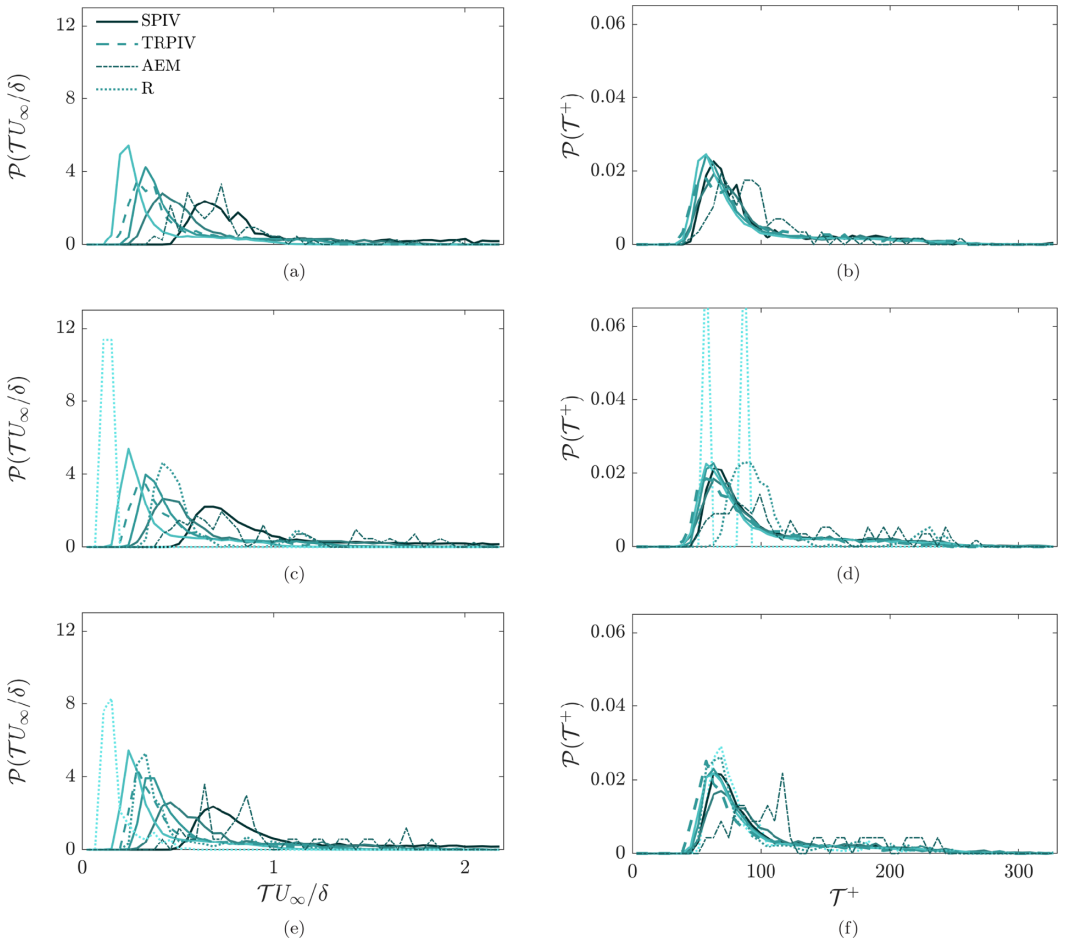

FIG. 10. PDF of $\mathcal{T}(U_m)$, as defined in Fig. 7. Outer (left) and inner (right) scaling for $0.63 \leqslant U_m/U_\infty \leqslant 0.66$ (a), (b); $0.72 \leqslant U_m/U_\infty \leqslant 0.75$ (c), (d); and $0.81 \leqslant U_m/U_\infty \leqslant 0.84$ (e), (f). Increasing Re_τ is denoted with lighter colors.

aside from deviations in the peak shape—and particularly the drop-off level of the maximum values discussed above (Fig. 9)—the use of a uniform convection velocity for the comparison between time-resolved and snapshot data was not seen to influence any of the scaling results for $\mathcal{T}$ presented here.

The overall behavior of $\langle\mathcal{T}\rangle$ with increasing U_m accentuates the discrepancies discussed above between the models, while it also indicates the slight increase of temporal coherence for higher modal velocities (Fig. 12; a similar observation was made by Laskari *et al.* [16]), although care should be taken when comparing the two studies, given the different definitions of temporal coherence followed in each.

V. SUMMARY AND DISCUSSION

From the above analysis, the robustness of the observed patterns and UMZ peak morphology in time, as well as the success of inner scaling in sufficiently collapsing most relevant metrics, are the most compelling conclusions. Despite observed discrepancies, the overall agreement between data

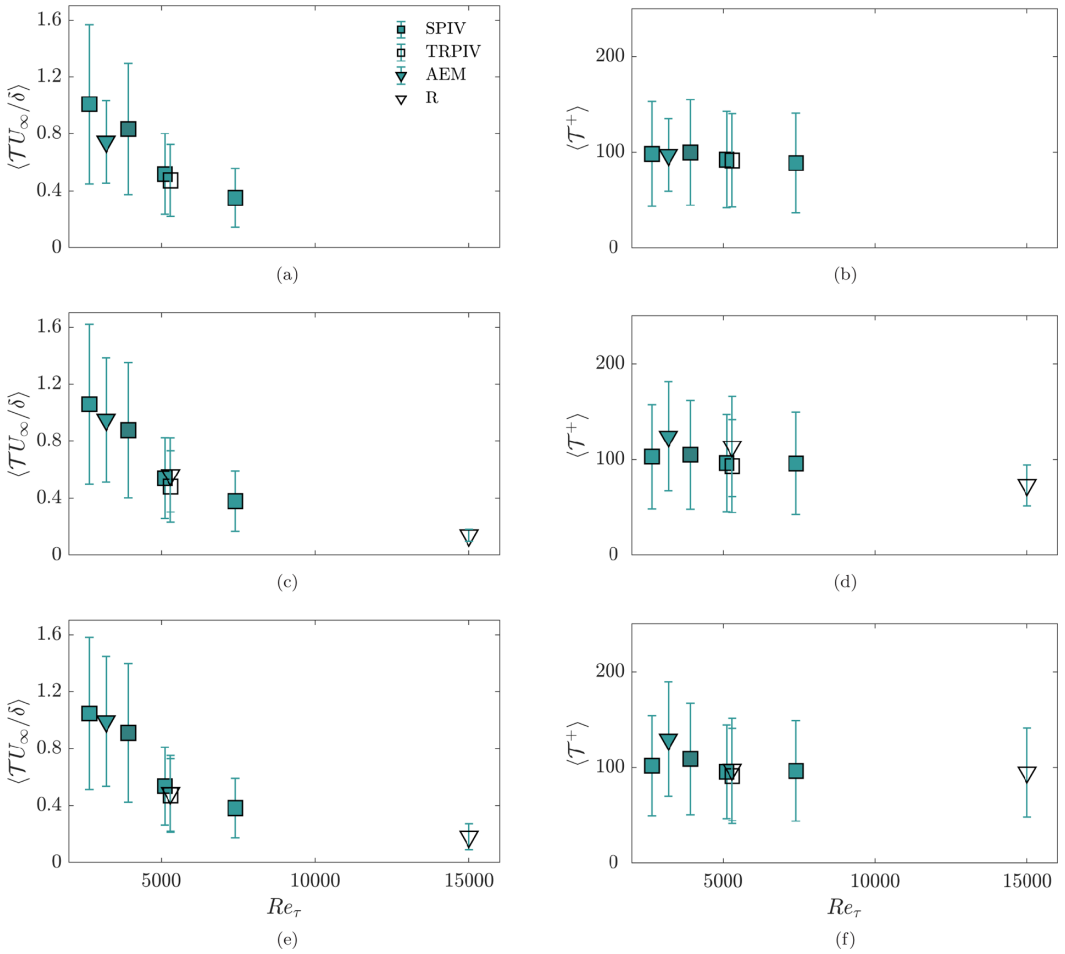

FIG. 11. Variation of $\langle \mathcal{T}(U_m) \rangle$ with Re_τ in outer (left) and inner (right) scaling, for $0.63 \leqslant U_m/U_\infty \leqslant 0.66$ (a), (b); $0.72 \leqslant U_m/U_\infty \leqslant 0.75$ (c), (d); and $0.81 \leqslant U_m/U_\infty \leqslant 0.84$ (e), (f). Error bars equal one standard deviation.

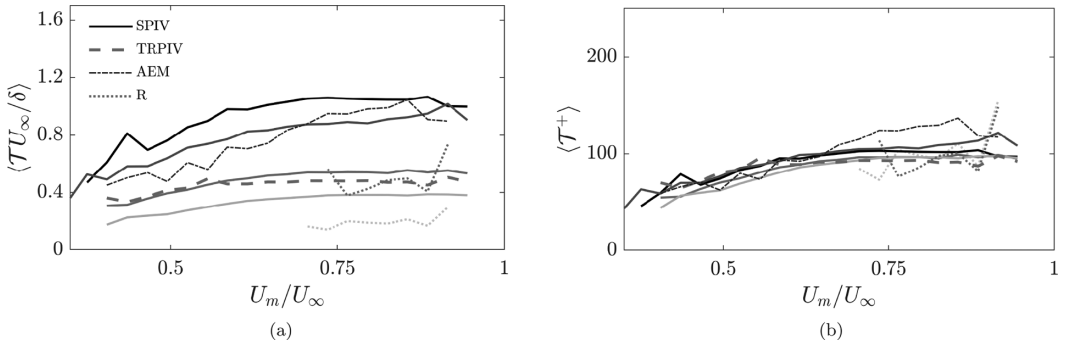

FIG. 12. Variation of $\langle \mathcal{T} \rangle$ with U_m in outer (a) and inner (b) scaling. Increasing Re_τ is denoted with lighter colours.

sets is notable in both mean values and distributions, especially given the variety on input data and the effort made to ensure consistency of the PDF construction process and analysis.

With respect to scaling, it should be noted again here that we focus entirely on structures anchored within the logarithmic region for all the modeling data sets, where we expect specific scaling relationships based on self-similarity and we can ensure the most equitable comparison between the models. The preceding analysis on the temporal characteristics of the streamwise velocity PDF, including the full-scale experimental data sets, supports inner normalization for a collapse of most metrics. While it seems that ruling out outer normalization is certainly justifiable, it should be stressed that the range of Reynolds numbers available might not be sufficient for a definite conclusion on whether mixed scaling would be more suitable than inner scaling tested here. The highest available Reynolds number belongs to a synthetic data set (R2), which was constructed using a particularly discrete frequency input, localized in the logarithmic region. As such, the range of Reynolds numbers in the available data sets certainly allows assessment of the two models in replicating the experimental features (and to some extent the observed scaling), however, full-scale experimental data sets with a wider Reynolds number range would be required to fully assess scaling behavior.

The experimental data sets indicated only marginal discrepancies due to the space-time conversion, even considering a uniform convection velocity in y. A higher drop-off level of the UMZ maximum peak value for the time-resolved data sets (Fig. 9) was the only metric where appreciable variation was observed within the different experimental databases, however, given also the lack of any clear Reynolds number scaling for this metric, more in-depth analysis would be required for further conclusions on the observed behavior. Regarding the selection of convection velocity itself, as mentioned in Sec. III, a wall-normal dependence for U_c was also tested for the AEM data set and the differences in the metrics presented here were minimal. For that particular evaluation, the PDF construction process for the AEM was similar to that for the time-resolved data sets (see Fig. 1), with periodic boundary conditions. For consistency, all data sets were also down-sampled to match the resulting temporal resolution ($dt^+ \approx 32$) of the AEM, allowing for an additional evaluation of potential resolution effects in the trends discussed here; all effects were again shown to be inconsequential and the main trends unaltered. For completeness, different uniform convection velocities were also tested for both SPIV and AEM data sets, again with only marginal differences observed. Besides space-time conversion, the experimental databases used here (SPIV) further highlighted that a different flow geometry (channel or external boundary layer) also has negligible influence on the resulting characteristics. This observation further cements our conclusions with respect to the model data sets (outlined in the following paragraph); it is the model construction and input selection rather than the flow geometry that leads to the discrepancies between the resolvent (channel) and the AEM (TBL) datasets.

Finally, with respect to model comparisons, different benefits and drawbacks of each were displayed, although the resulting conclusions presented herein apply exclusively on reproducing the temporal characteristics of $\mathcal{P}(U,t)$ and are not necessarily representative of global model performance. Synthetic data sets based on the resolvent framework have been shown to successfully replicate the characteristics of the PDF transitions [3]. In the present paper, these findings were extended to show that for modal velocities at the outer edge of the log region, the resulting temporal coherence of UMZ peaks and Reynolds number scaling was also in good agreement with the experimentally observed behaviours. On the other hand, these data sets were limited by the discrete frequency input, inherent in the model construction, reflected in a restriction of PDF patterns within a narrow range of velocities (see, for example, Fig. 2) and a resulting sparser value distribution for the transition rates ϕ_- and ϕ^+ [Fig. 4(a)] and a shorter wall-normal extent in the conditionally averaged fluctuations (Fig. 5); temporal coherence of UMZ peaks also quickly deteriorated for velocities closer to the wall and very close to the free stream (Fig. 12). Regarding the synthetic data set based on the AEM, the broadband frequency input of the model allowed a much broader range of velocities with substantial PDF activity compared to the resolvent data sets, reflected in the smoother distribution of transition rates ϕ_- and ϕ^+ and the wider wall-normal extent of the conditionally

averaged fluctuating velocity. However, the instantaneous structure details encompassed in the AEM also resulted in significant discrepancies in the temporal behavior of the model when compared to experimental data, with respect to both the phase and the geometry of the conditional structures (Fig. 5), which could be traced back to a much less prominent peak behavior in $\mathcal{P}(U,t)$ [Figs. 2 and 6(d)], with PDF values almost monotonically decreasing with decreasing velocity. This was also reflected in the disparities observed in the temporal coherence of the UMZ peaks for the AEM, which was shown to be larger on average and with a more discrete distribution of values than either the experimental or the resolvent-based data sets. Aside from the lack of a well-defined instantaneous structure, another potential explanation for the observed discrepancies in the AEM is an increase in the number of vectors belonging to higher velocities: The largest eddies of the nested packets occupy a much larger proportion of the flow field, averaging out larger velocity deficits from smaller eddies which have a more limited wall-normal extent.

VI. CONCLUSIONS

The temporal characteristics of the PDF of the streamwise velocity were evaluated in a variety of experimental and synthetic data sets of wall-bounded flows, the latter based on the attached eddy model (AEM [2]) and the resolvent framework [1]. The effects of Reynolds number, availability of temporal information, and specifics of model construction were assessed. The temporal patterns in $\mathcal{P}(U,t)$, first analyzed by Laskari and McKeon [3], were seen to be robust and repeatable in all data sets. The rate of transitions, ϕ, and the temporal coherence of UMZ peaks are both found to scale in inner units. The use of a uniform convection velocity in space-to-time transformations as well as the specific flow geometry (internal versus external) both had a negligible effect in most metrics analyzed here. Overall, the two synthetic data sets were able to replicate many of the experimentally observed behaviors, with a narrow frequency input and lack of instantaneous structural details being the main drawbacks for the resolvent and AEM-based data sets, respectively.

ACKNOWLEDGMENT

The support of ONR through Grant No. N00014-17-1-3022 (A.L., B.J.M.) is gratefully acknowledged.

[1] B. J. McKeon and A. S. Sharma, A critical-layer framework for turbulent pipe flow, J. Fluid Mech. **658**, 336 (2010).
[2] A. E. Perry and M. S. Chong, On the mechanism of wall turbulence, J. Fluid Mech. **119**, 173 (1982).
[3] A. Laskari and B. J. McKeon, Temporal characteristics of the probability density function of velocity in wall-bounded turbulent flows, J. Fluid Mech. **913**, A6 (2021).
[4] C. D. Meinhart and R. J. Adrian, On the existence of uniform momentum zones in a turbulent boundary layer, Phys. Fluids **7**, 694 (1995).
[5] R. J. Adrian, C. D. Meinhart, and C. Tomkins, Vortex organization in the outer region of the turbulent boundary layer, J. Fluid Mech. **422**, 1 (2000).
[6] J. Eisma, J. Westerweel, G. Ooms, and G. E. Elsinga, Interfaces and internal layers in a turbulent boundary layer, Phys. Fluids **27**, 055103 (2015).
[7] C. M. de Silva, J. Philip, N. Hutchins, and I. Marusic, Interfaces of uniform momentum zones in turbulent boundary layers, J. Fluid Mech. **820**, 451 (2017).
[8] B. J. Balakumar and R. J. Adrian, Large- and very-large-scale motions in channel and boundary-layer flows, Philos. Trans. R. Soc. A **365**, 665 (2007).
[9] N. Hutchins and I. Marusic, Evidence of very long meandering features in the logarithmic region of turbulent boundary layers, J. Fluid Mech. **579**, 1 (2007).

[10] M. Guala, S. E. Hommema, and R. J. Adrian, Large-scale and very-large-scale motions in turbulent pipe flow, J. Fluid Mech. **554**, 521 (2006).
[11] J. P. Monty, N. Hutchins, H. C. H. Ng, I. Marusic, and M. S. Chong, A comparison of turbulent pipe, channel and boundary layer flows, J. Fluid Mech. **632**, 431 (2009).
[12] W. Li, D. Roggenkamp, V. Paakkari, M. Klaas, J. Soria, and W. Schröder, Analysis of a drag reduced flat plate turbulent boundary layer via uniform momentum zones, Aerosp. Sci. Technol. **96**, 105552 (2020).
[13] Y. Farsiani, Z. Saeed, B. Jayaraman, and B. Elbing, Modification of turbulent boundary layer coherent structures with drag reducing polymer solution, Phys. Fluids **32**, 015107 (2020).
[14] C. M. de Silva, N. Hutchins, and I. Marusic, Uniform momentum zones in turbulent boundary layers, J. Fluid Mech. **786**, 309 (2016).
[15] T. Saxton-Fox and B. J. McKeon, Coherent structures, uniform momentum zones and the streamwise energy spectrum in wall-bounded turbulent flows, J. Fluid Mech. **826**, R6 (2017).
[16] A. Laskari, R. de Kat, R. J. Hearst, and B. Ganapathisubramani, Time evolution of uniform momentum zones in a turbulent boundary layer, J. Fluid Mech. **842**, 554 (2018).
[17] K. Wang, L. Biahui, and L. Liu, Experimental measurement of coherent structures in turbulent boundary layers using moving time-resolved particle image velocimetry, Phys. Fluids **32**, 115102 (2020).
[18] M. Heisel, C. M. De Silva, N. Hutchins, I. Marusic, and M. Guala, On the mixing length eddies and logarithmic mean velocity profile in wall turbulence, J. Fluid Mech. **887**, R1 (2020).
[19] R. J. Hearst, C. M. de Silva, E. Dogan, and B. Ganapathisubramani, Uniform-momentum zones in a turbulent boundary layer subjected to freestream turbulence, J. Fluid Mech. **915**, A109 (2021).
[20] M. Bross, T. Fuchs, and C. J. Kähler, Interaction of coherent flow structures in adverse pressure gradient turbulent boundary layers, J. Fluid Mech. **873**, 287 (2019).
[21] A. Thavamani, C. Cuvier, C. Willert, J. M. Foucaut, C. Atkinson, and J. Soria, Characterisation of uniform momentum zones in adverse pressure gradient turbulent boundary layers, Exp. Therm. Fluid Sci. **115**, 110080 (2020).
[22] O. J. Williams, D. Sahoo, M. L. Baumgartner, and A. J. Smits, Experiments on the structure and scaling of hypersonic turbulent boundary layers, J. Fluid Mech. **834**, 237 (2018).
[23] M. Gul, G. E. Elsinga, and J. Westerweel, Internal shear layers and edges of uniform momentum zones in a turbulent pipe flow, J. Fluid Mech. **901**, A10 (2020).
[24] S. C. Morris, S. R. Stolpa, P. E. Slaboch, and J. C. Klewicki, Near-surface particle image velocimetry measurements in a transitionally rough-wall atmospheric boundary layer, J. Fluid Mech. **580**, 319 (2007).
[25] M. Heisel, T. Dasari, Y. Liu, J. Hong, F. Coletti, and M. Guala, The spatial structure of the logarithmic region in very-high-Reynolds-number rough wall turbulent boundary layers, J. Fluid Mech. **857**, 704 (2018).
[26] S. Senthil, C. Atkinson, and J. Soria, Analysis of the spanwise extent and time persistence of uniform momentum zones in zero pressure gradient and adverse pressure gradient turbulent boundary layers, J. Phys.: Conf. Ser. **1522**, 012013 (2020).
[27] X. Chen, Y. M. Chung, and M. Wan, Uniform-momentum zones in a turbulent pipe flow, J. Fluid Mech. **884**, A25 (2020).
[28] X. Chen, Y. M. Chung, and M. Wan, The uniform-momentum zones and internal shear layers in turbulent pipe flows at Reynolds numbers up to $Re_\tau = 1000$, Int. J. Heat Fluid Flow **90**, 108817 (2021).
[29] G. Taylor, The spectrum of turbulence, Proc. R. Soc. Lond. A. **164**, 476 (1938).
[30] J. C. C. Bautista, A. Ebadi, C. M. White, G. P. Chini, and J. C. Klewicki, A uniform momentum zone-vortical fissure model of the turbulent boundary layer, J. Fluid Mech. **858**, 609 (2019).
[31] F. Eich, C. M. de Silva, I. Marusic, and C. J. Kähler, Towards an improved spatial representation of a boundary layer from the attached eddy model, Phys. Rev. Fluids **5**, 034601 (2020).
[32] A. S. Sharma and B. J. McKeon, On coherent structure in wall turbulence, J. Fluid Mech. **728**, 196 (2013).
[33] G. P. Chini, B. Montemuro, C. M. White, and J. Clewicki, A self-sustaining process model of inertial layer dynamics in high Reynolds number turbulent wall flows, Philos. Trans. R. Soc. A. **375**, 20160090 (2017).

[34] B. Montemuro, C. M. White, J. Clewicki, and G. P. Chini, A self-sustaining process theory for uniform momentum zones and internal shear layers in high Reynolds number shear flows, J. Fluid Mech. **901**, A28 (2017).
[35] B. J. McKeon, Self-similar hierarchies and attached eddies, Phys. Rev. Fluids **4**, 082601(R) (2019).
[36] C. M. de Silva, D. T. Squire, N. Hutchins, and I. Marusic, Towards capturing large scale coherent structures in boundary layers using particle image velocimetry, in *Proceedings of the 7th Australian Conference on Laser Diagnostics in Fluid Mechanics and Combustion, Melbourne, Australia* (2015), pp. 1–4.
[37] F. H. Clauser, Turbulent boundary layers in adverse pressure gradients, J. Aeronaut. Sci. **21**, 91 (1954).
[38] K. A. Chauhan, P. A. Monkewitz, and H. M. Nagib, Criteria for assessing experiments in zero pressure gradient boundary layers, Fluid Dyn. Res. **41**, 021404 (2009).
[39] Y. S. Kwon, J. Philip, C. M. de Silva, N. Hutchins, and J. P. Monty, The quiescent core of turbulent channel flow, J. Fluid Mech. **751**, 228 (2014).
[40] C. M. de Silva, E. P. Gnanamanickam, C. Atkinson, N. A. Buchmann, N. Hutchins, J. Soria, and I. Marusic, High spatial range velocity measurements in a high Reynolds number turbulent boundary layer, Phys. Fluids **26**, 025117 (2014).
[41] B. J. McKeon, The engine behind (wall) turbulence: perspectives on scale interactions, J. Fluid Mech. **817**, P1 (2017).
[42] I. Marusic, J. P. Monty, M. Hultmark, and A. J. Smits, On the logarithmic region in wall turbulence, J. Fluid Mech. **716**, R3 (2013).
[43] R. Moarref, A. S. Sharma, T. J. A., and B. J. McKeon, Model-based scaling of the streamwise energy density in high-Reynolds-number turbulent channels, J. Fluid Mech. **734**, 275 (2013).
[44] J. D. Woodcock and I. Marusic, The statistical behaviour of attached eddies, Phys. Fluids **27**, 015104 (2015).
[45] K. B. M. Q. Zaman and A. K. M. F. Hussain, Taylor hypothesis and large-scale coherent structures, J. Fluid Mech. **112**, 379 (1981).
[46] K. Chauhan, J. Philip, C. C. M. de Silva, N. Hutchins, and I. Marusic, The turbulent/non-turbulent interface and entrainment in a boundary layer, J. Fluid Mech. **742**, 119 (2014).
[47] D. Fan, J. Xu, M. X. Yao, and J.-P. Hickey, On the detection of internal interfacial layers in turbulent flows, J. Fluid Mech. **872**, 198 (2019).